Research Square

Preprints are preliminary reports that have not undergone peer review.
They should not be considered conclusive, used to inform clinical practice,
or referenced by the media as validated information.

A tunable Synthetic Vascularized Eye Fundus for patient-free retinal imaging validation

Valentina Capalbo

valentina.capalbo@iit.it

D-Tails s.r.l. S.B.

Giada Grasso

Sapienza University of Rome

Zita Zita Salajkov´a

D-Tails s.r.l. S.B.

Ojus Bagal

D-Tails s.r.l. S.B.

Maria Grazia Gambarota

Center for Life Nano- & Neuro-Science, Italian Institute of Technology

Manolo Gianvanni

Center for Life Nano- & Neuro-Science, Italian Institute of Technology

Martina Fioretti

D-Tails s.r.l. S.B.

Asia Zanetti

D-Tails s.r.l. S.B.

Maryamsadat Ghoreishi

D-Tails s.r.l. S.B.

Riccardo Reale

University of Rome Tor Vergata

Ylenia Gigante

D-Tails s.r.l. S.B.

Silvia Di Angelantonio

Center for Life Nano- & Neuro-Science, Italian Institute of Technology

Giancarlo Ruocco

Center for Life Nano- & Neuro-Science, Italian Institute of Technology

Marco Leonetti

National Research Council

Article

Keywords: Biomedical optics, Retinal imaging, Eye phantom, Microfluidics, Image registration, Fluorescence imaging

Posted Date: September 23rd, 2026

DOI: https://doi.org/10.21203/rs.3.rs-11129073/v1

License: This work is licensed under a Creative Commons Attribution 4.0 International License. Read Full License

Additional Declarations: No competing interests reported.

A tunable Synthetic Vascularized Eye Fundus for patient-free retinal imaging validation

Valentina Capalbo[1,2*†], Giada Grasso[3,2†], Zita Salajková[1,2], Ojus Bagal[1,2], Maria Grazia Gambarota[2], Manolo Gianvanni[2], Martina Fioretti[1,2], Asia Zanetti[1,2], Maryamsadat Ghoreishi[1,2], Riccardo Reale[4], Ylenia Gigante[1,2], Silvia Di Angelantonio[2,1,5], Giancarlo Ruocco[2,6], Marco Leonetti[7,2,1]

[1*]D-Tails s.r.l. S.B., Via Agrigento 4A/4B, Rome, 00161, Italy.
[2]Center for Life Nano- & Neuro-Science, Italian Institute of Technology, Viale Regina Elena 291, Rome, 00161, Italy.
[3]Department of Chemistry and Technologies of Drugs, Sapienza University of Rome, Piazzale Aldo Moro 5, Rome, 00185, Italy.
[4]Department of Civil Engineering and Computer Science, University of Rome Tor Vergata, Rome, Italy.
[5]Department of Physiology and Pharmacology, Sapienza University of Rome, Piazzale Aldo Moro 5, Rome, 00185, Italy.
[6]Department of Physics, Sapienza University of Rome, Piazzale Aldo Moro 5, Rome, 00185, Italy.
[7]Institute of Nanotechnology of the National Research Council of Italy, CNR-NANOTEC, Piazzale Aldo Moro 5, Rome, 00185, Italy.

*Corresponding author(s). E-mail(s): valentina.capalbo@iit.it;
†These authors contributed equally to this work.

Abstract

The validation of novel retinal imaging techniques and motion-correction algorithms is often constrained by biological variability and the lack of ground-truth data in *in vivo* measurements. To address this limitation, patient-free validation platforms require standardized targets that mimic selected optical and structural properties of the human eye. Here, we present a Synthetic Vascularized Eye Fundus (SVEF), a perfusable and contrast-tunable microfluidic insert designed for ophthalmic eye phantom platforms. The SVEF features a high-density, retinal-like vascular network fabricated by soft lithography using a

custom polydimethylsiloxane-zinc oxide (PDMS–ZnO) composite. This substrate acts as a bright, diffusely scattering background, while perfusion with hemoglobin solutions generates physiologically relevant absorbing vessel-like structures. By optimizing the hemoglobin concentration, we achieved a vessel-to-background contrast closely matching that of *in vivo* human fundus images. We validated the SVEF as a robust structural reference for image registration, demonstrating accurate retrieval of imposed saccade-like micro-displacements and enabling the enhancement of multi-frame fluorescence imaging. Finally, we confirmed the compatibility of the device with biological assays by successfully integrating and imaging human iPSC-derived retinal neurons. The SVEF provides a reproducible, patient-free environment for benchmarking ophthalmoscopic systems, optimizing image-registration pipelines and supporting versatile *in vitro* retinal experiments.

Keywords: Biomedical optics, Retinal imaging, Eye phantom, Microfluidics, Image registration, Fluorescence imaging

1 Introduction

Imaging of the retinal vasculature is widely used to diagnose and monitor ocular diseases and is increasingly investigated as a tool to identify biomarkers associated with systemic and neurological disorders [1–3]. Beyond ophthalmology, the retina has gained increasing attention as an accessible extension of the central nervous system, offering a unique opportunity for non-invasive assessment of structural, vascular and functional alterations. These features have accelerated the development of retinal imaging techniques aimed at improving spatial resolution, contrast sensitivity and quantitative reproducibility under clinically relevant imaging conditions. Several imaging methods are currently used for retinal assessment. Fluorescence-based angiography techniques are reference tools for vascular evaluation. Examples include fundus autofluorescence imaging [4, 5] and targeted molecular fluorescence approaches [6–8], which are explored to access biochemical and pathological information that is not directly available from purely structural imaging. Label-free techniques, which typically do not require staining, such as optical coherence tomography (OCT) and OCT angiography (OCTA), instead provide non-invasive structural and vascular contrast and have become central to routine clinical practice [9].

Across these modalities, retinal image quality remains constrained by the optical properties of the eye [10]. The limited numerical aperture and aberrations of the ocular system can reduce spatial resolution and contrast, while involuntary eye movements during acquisition can introduce frame misalignment, motion-related artefacts and image blur, particularly in scanning imaging and multi-frame acquisition [11, 12]. Image registration is therefore widely used in retinal imaging to estimate inter-frame motion and to correct or mitigate these artefacts [13, 14]. Several registration techniques have been developed for this purpose. Among them, feature-based methods are widely employed because they estimate the geometrical transformation occurring between different acquisitions by identifying and matching distinct anatomical landmarks [15]. These latter are commonly derived from the vascular network

and include vessel bifurcations, intersections and other characteristic vascular structures. Once the images have been aligned, multiple acquisitions can be combined or averaged to improve signal-to-noise ratio, enhance structural visibility and support quantitative comparisons. However, the development and objective validation of these techniques are often limited by the lack of controlled datasets with known ground-truth displacements.

In general, the validation of retinal imaging systems into robust diagnostic tools requires extensive validation. *In vivo* measurements are essential for clinical translation, but they are affected by biological variability and limited experimental controllability. Patient-free validation platforms can therefore play a crucial role in benchmarking imaging systems, optimizing acquisition parameters and quantifying performance under reproducible conditions.

Several phantom devices have been proposed to mimic retinal and eye anatomical and optical properties, providing standardized targets for calibration and method comparison [16–22]. However, most of these eye phantoms (EP) have been primarily conceived for OCT/OCTA validation tasks. Recently, Ferraro et al. introduced the Bio-Imaging Model Eye (BIME), a EP platform designed to reproduce a human-like ophthalmic environment while accommodating biological samples and controlled eye-like (saccade) motion [23]. This type of platform provides a realistic optical interface for different retinal imaging experiments and represents a suitable environment for testing synthetic fundus inserts.

Here, we present a Synthetic Vascularized Eye Fundus (SVEF) designed as a perfusable and contrast-tunable fundus insert for ophthalmic EP platforms such as BIME. The SVEF consists of a retinal-like microfluidic vascular network fabricated by photolithography and soft lithography [24]. These microfabrication techniques, in fact, allow to realize a device with feature size comparable to human physiological microvasculature [25]. The SVEF is replicated in polydimethylsiloxane (PDMS)—a silicone elastomer widely used in soft lithography [26, 27]—modified with Zinc Oxide (ZnO) nanoparticles (PDMS–ZnO composite) [28, 29] and perfused with hemoglobin-based solutions. The PDMS–ZnO substrate provides a bright diffuse background under reflectance illumination, while the hemoglobin-filled microchannels act as absorbing vessel-like structures. By varying the hemoglobin concentration, the vessel-to-background contrast can be tuned to reproduce contrast values comparable to those observed in human fundus images. In addition, it can serve as a structural reference for implementation and validation of image registration techniques. The SVEF provides a reproducible structural and optical reference in which vascular contrast can be controlled and potentially exploited for testing different retinal-focused experiments. The strength of this device lies in achieving these results circumventing the difficulties associated with reproducing the full biological, spectral and optical complexity of the eye.

In this work, we describe the design and fabrication of the device, compare standard PDMS and PDMS–ZnO substrates, optimize hemoglobin perfusion to obtain fundus-like vascular contrast and validate the resulting microchannel dimensions. We further assess the use of the vascular pattern as a reference for image acquisition and

registration, supporting the potential application of SVEF in motion-correction and multi-frame retinal imaging workflows aimed at resolution enhancement.

2 Results

To evaluate the SVEF as a functional insert for EP imaging, we characterized the device according to three main requirements: reproducible fabrication of a retinal-like vascular pattern, generation of tunable vessel-to-background contrast, and usability as a structural reference within the BIME platform. The following results show how the fabricated microfluidic network behaves under reflectance and fluorescence imaging conditions, and assess its suitability for patient-free retinal imaging experiments.

2.1 Design and fabrication of the SVEF

The SVEF was realized through a photolithography-based master molding workflow followed by soft lithography replication, enabling the reproducible fabrication of a high-density retinal-like vascular network. Details of the fabrication procedure are reported in the Methods section. Our workflow followed standard protocols for microfluidic fabrication [24]; the vascular layout was first designed as a 2D CAD pattern and converted into a high-resolution photomask. The pattern was then replicated into a negative SU-8 photoresist layer [30] to generate a master mold, which served as a template for producing perfusable elastomeric replicas. Figure 1 summarizes these fabrication steps, from the CAD design to the final perfused SVEF device.

The device was designed as a 12-mm diameter fundus-like insert compatible with the BIME sample holder [23]. The vascular architecture consisted of vessel-like microchannels distributed across the circular footprint, with a high-density grid integrated in the central region. This grid was introduced to provide a dense set of well-defined intersections within the imaging field of view. Such reference points are expected to facilitate image alignment, frame-to-frame registration and spatial co-localization with fluorescent targets, such as labelled cells or localized fluorescent features. To improve perfusion of the microfluidic network, the channels were designed with open-ended outlets. During filling, these open ends allowed the hemoglobin solution to displace air from the channels, thereby promoting complete filling of the vascular network and reducing the formation of trapped air pockets. Once the channels were filled, the open ends were sealed with optical glue to retain the hemoglobin solution inside the device during imaging experiments. Figure 1 clearly shows that, after development, the SU-8 master preserved both the vascular features and the central grid, indicating that the photolithographic process was suitable for reproducing the critical microscale structures (~ 20 μm) required for the SVEF design.

Replicas were fabricated using a PDMS–ZnO composite rather than standard transparent PDMS. Pure PDMS, in fact, produces limited backscattered signal in reflectance imaging, which reduces the visibility of absorbing microchannels. The addition of ZnO nanoparticles increases light scattering within the elastomeric substrate, due to the higher refractive index of ZnO ($n_{ZnO} \sim 2$) with respect to that of PDMS ($n_{PDMS} \sim 1.41$) [31, 32]. The result is an opaque, diffusely reflecting substrate that appears as a bright background, against which the hemoglobin-filled, highly absorbing

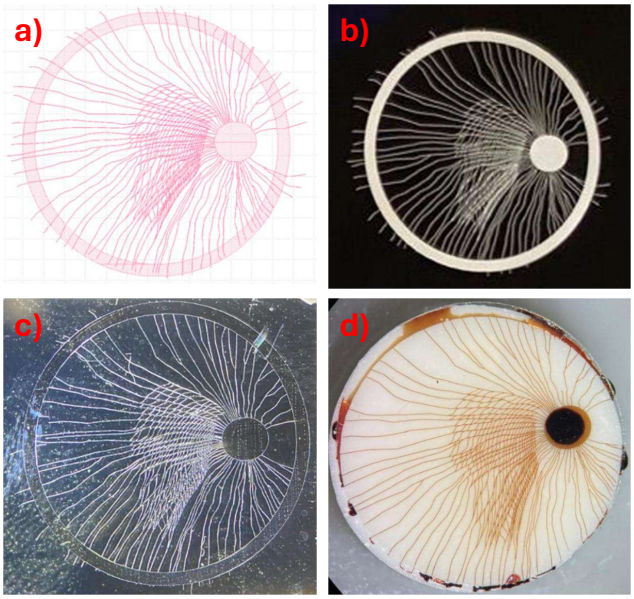


Fig. 1 Overview of the main SVEF fabrication steps. **a)** CAD layout of the retinal-like microvascular network with central high-density grid and circular chip footprint. **b)** High-resolution film photomask used for UV pattern transfer. **c)** SU-8 master mold obtained from photolithography. **d)** Final chip realized with PDMS-ZnO composite and perfused with hemoglobin.

channels appear as dark structures. Note that the purpose of the PDMS–ZnO substrate was not to reproduce the full optical complexity or spectral background of the human fundus. Rather, it was designed to provide a stable scattering background that yields vessel-to-background contrast comparable to that observed in fundus imaging, ensuring reliable visualization of the perfused vascular network. The effect of the scattering substrate on vessel visibility was evaluated by comparing two SVEF prototypes fabricated with standard PDMS and PDMS–ZnO, respectively. Both devices were perfused with the same hemoglobin-based solution, assembled within the BIME and imaged under identical LED reflectance illumination using the optical setup described in Fusco et. al [33] (see panel h) in Fig.1). This controlled configuration was chosen to isolate the contribution of the substrate material to the observed vessel contrast. As shown in Figure 2, the PDMS-only device produced weak vascular contrast because the transparent substrate did not efficiently backscatter the incident light. In contrast, the PDMS–ZnO device generated a bright diffuse background against which the absorbing microchannels appeared as well-defined dark vessel-like structures.

2.2 Optimization of vascular contrast using hemoglobin perfusion

After establishing the PDMS–ZnO composite as a suitable substrate for generating a scattering background, the hemoglobin concentration was optimized to reproduce the vessel-to-background contrast observed in human fundus images. Hemoglobin was

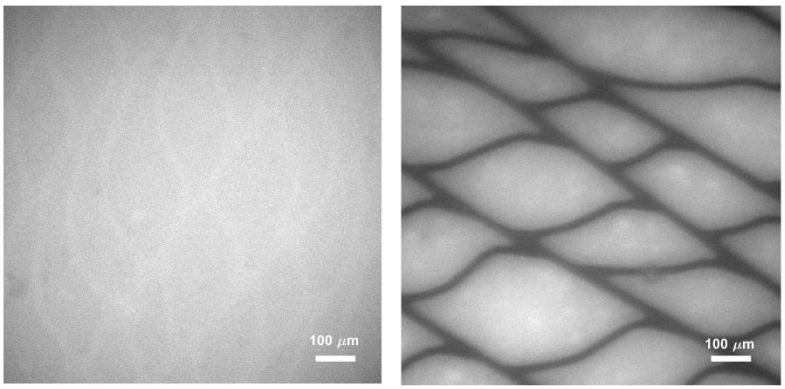


Fig. 2 Comparison of SVEF devices fabricated using standard PDMS (left) and a PDMS–ZnO composite (right). Both devices were perfused with the same hemoglobin solution and imaged under identical optical conditions (LED reflectance illumination). The addition of ZnO nanoparticles produces a bright scattering background, resulting in enhanced vessel-to-background contrast. Scale bars are 100 μm.

selected as the absorbing medium because blood absorption in the visible spectral range is mainly governed by hemoglobin concentration and oxygenation state, with oxy- and deoxy-hemoglobin exhibiting characteristic absorption bands in this wavelength region [34, 35]. When confined within the microfluidic network, the hemoglobin solution enables the vascular channels to appear as dark structures against the bright scattering background generated by the PDMS–ZnO substrate. In addition, its macromolecular nature promotes stable confinement within the microchannels, supporting sharp and persistent definition of the vascular pattern during imaging compared with low-molecular-weight dyes, which may progressively diffuse or blur in PDMS-based devices. The purpose of this analysis was not to reproduce the complete optical properties of whole blood or the full spectral complexity of the human fundus. Rather, we aimed to identify a hemoglobin concentration that produced vessel-to-background contrast comparable to that observed in human fundus imaging, since this parameter directly affects the ability of retinal imaging systems to resolve fine vascular details.

In adult human blood, hemoglobin concentration is typically approximately 12–18 g/dL, corresponding to about 1.9–2.8 mM when expressed as tetrameric hemoglobin using a molecular weight of 64.5 kDa [36]. Based on this physiological reference range, three hemoglobin concentrations were tested: 2, 2.5 and 3 mM. The corresponding solutions were prepared in distilled water and used to perfuse the SVEF devices, as described in the Methods section. The perfused devices were assembled within the BIME and imaged using the fundus imaging module described by Salajková et al. [3]. Their vascular contrast was compared with that measured in a representative *in vivo* human fundus image acquired using the same imaging configuration. Figure 3 shows representative human and SVEF fundus images.

Vessel contrast was quantified as

$$C = \frac{I_{\mathrm{bkg}} - I_{\mathrm{vessel}}}{I_{\mathrm{bkg}}}, \tag{1}$$

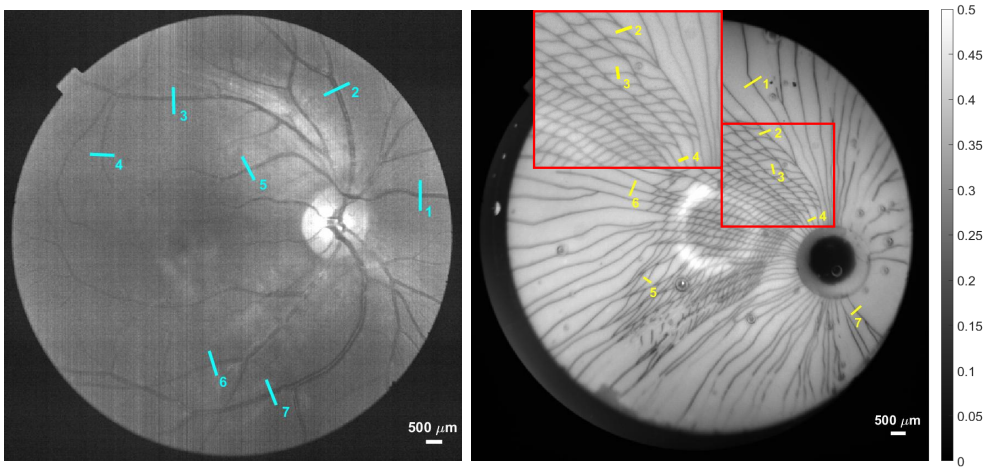


Fig. 3 Comparison of a representative human fundus image (left) and a SVEF image acquired after perfusion with a 2 mM hemoglobin solution (right). Cyan and yellow lines indicate the vessels selected for contrast analysis in the human fundus and SVEF images, respectively. In particular, transverse intensity profiles were extracted approximately perpendicular to the vessel axis. In the right panel, red boxes show a zoom-in of a region containing the dense microchannel network realized for the SVEF. Small circular dark features in the image correspond to air bubbles trapped within the BIME chamber, whereas the central bright annulus originates from specular reflection of the ophthalmoscope illumination at the glass coverslip used to seal the microfluidic device. Some peripheral regions appear to be incompletely perfused; regions affected by bubbles, reflections or incomplete filling were excluded from the quantitative analysis. Scale bars are 500 μm.

where I_{bkg} is the local background intensity surrounding the vessel and I_{vessel} is the intensity measured within the vessel region. Since vessels appear as dark features in the images, I_{vessel} was estimated from the minimum intensity within the central vessel region. The same criterion was applied to both the SVEF and human fundus images. To evaluate the vessel contrast we selected different vessels and extracted the respective transverse intensity profiles, avoiding bifurcations, crossings and regions with non-uniform illumination whenever possible. The profiles analysed are indicated by the coloured lines in Figure 3, and the corresponding contrast values are shown in Figure 4. Table 1 reports the mean values for the cases analysed. The human fundus image yielded a mean vessel contrast of 0.20 ± 0.05. Among the tested SVEF conditions, the 2mM hemoglobin solution produced the closest agreement with the human fundus reference. This concentration was therefore selected for final perfusion of the device, as it provided clear visualization of the microvascular network while preserving a human fundus-like contrast level.

2.3 Assessment of microchannel dimensions

To characterize the dimensions of the fabricated vascular network, we performed a post-fabrication morphometric analysis of the SVEF perfused with the hemoglobin solution selected above. In particular, we refer to the microchannels already selected in the previous section (see the right panel in Figure 3). In photolithography-based

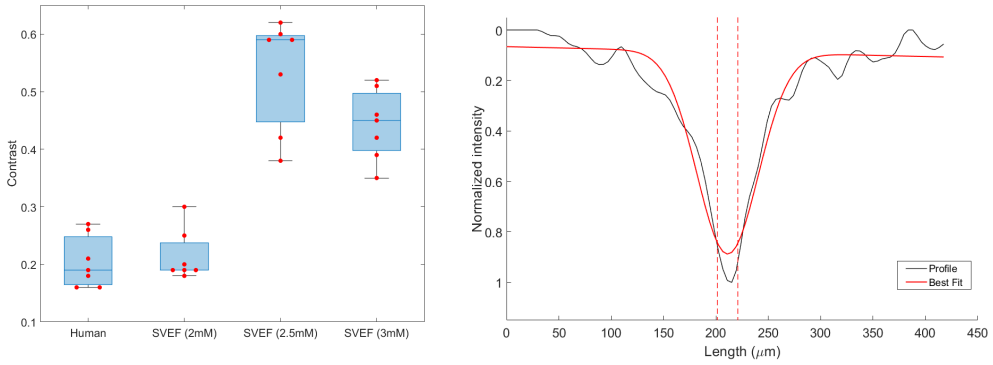


Fig. 4 *Left:* Vessel-to-background contrast measured in the human fundus image and in SVEF devices perfused with hemoglobin solutions at concentrations of 2, 2.5 and 3 mM. Red markers indicate the contrast values obtained for the individual analysed vessels, while the box plots summarize their distributions. The horizontal line within the box indicates the median value, while the whiskers are at 25th and 75th percentile. *Right:* Representative transverse intensity profile extracted across vessel 1 in the SVEF image shown in Figure 3. The solid black line represents the normalized measured profile, while the solid red line shows the best fit obtained using the double-edge model described in the Methods section. The red vertical dashed lines indicate the fitted channel-edge positions, corresponding to an apparent channel width of 19.6 μm.

Table 1 Vessel-to-background contrast measured in the human fundus image and in SVEF devices perfused with different hemoglobin concentrations. Reported values represent the mean $\pm$ standard deviation across $n = 7$ analysed vessels.

Image	Mean Contrast
Human fundus	0.20 ± 0.05
SVEF (2 mM hemoglobin)	0.21 ± 0.04
SVEF (2.5 mM hemoglobin)	0.50 ± 0.10
SVEF (3 mM hemoglobin)	0.44 ± 0.06

microfabrication, deviations from the nominal design may arise during pattern transfer, for example due to optical diffraction or scattering in the photoresist, and during replica molding, owing to elastomer curing and demolding. In addition, dimensions estimated from optical images can be affected by the spatial resolution and focusing characteristics of the imaging system. Here, vascular widths were quantified directly from the acquired images (see Figure 3) by analysing transverse intensity profiles across the selected microchannels. The right panel of Figure 4 shows a representative profile. Because the hemoglobin-filled channel appeared as a dark feature against the brighter PDMS–ZnO background, each profile was normalized to the local background and inverted before fitting. The resulting profile was fitted using a double-edge model representing the channel as a plateau bounded by two smooth transitions, as

described in the Methods section. The apparent channel width was defined as the distance between the two fitted edge positions. Across the seven analysed channels, the mean apparent width was 29 ± 13 μm (see Table 2). The relatively large dispersion of the measurement should not be interpreted solely as measurement uncertainty. As already mentioned, in addition to fabrication imperfections, the spatial resolution of the ophthalmoscopic system (here, ~ 10 μm), local defocus caused by imperfection alignment of the device with the imaging plane, and deviations of the extracted profiles from the direction perpendicular to the channel axis may broaden the measured profiles. However, it is clear that the measured widths agree with the size of small retinal vessels [25]. These results demonstrate that microscale vessel-like features remain resolvable after fabrication, perfusion and integration of the SVEF into the BIME. Thus, the analysis supports the suitability of the fabrication workflow for producing a model-eye-compatible synthetic vascular fundus.

2.4 Validation of motion tracking and image registration

Accurate image registration is an important requirement in retinal imaging because involuntary eye movements can introduce frame misalignment, motion-related artefacts and loss of image sharpness. More generally, registration enables the comparison, alignment and merging of images acquired at different times or with different imaging modalities. Retinal vessels are widely used as structural landmarks for image alignment because they represent a stable reference pattern across fundus images [13, 15]. Based on these considerations, we assessed whether the vascular pattern of the SVEF could serve as a reliable structural reference for motion retrieval under controlled and replicable imaging conditions.

As a first step, the SVEF device was mounted on motorized translation stages, and reflectance images were acquired using the LED optical setup already mentioned in the previous sections [33]. A sequence of 200 frames was recorded while random in-plane displacements were imposed within a 25×25 μm^2 range. The displacement of each frame relative to a fixed reference frame was estimated by cross-correlation of the vascular pattern using a custom MATLAB algorithm. The hemoglobin-filled microchannels remained consistently detectable throughout the sequence owing to their contrast against the scattering PDMS–ZnO background. The retrieved displacements showed a strong linear correspondence with the motor-imposed displacements along both axes, as shown in Figure 5. Linear regression yielded

$$X_{\text{shift}} = (0.968 \pm 0.004) X_{\text{motor}} - (0.624 \pm 0.027)\ \mu\text{m}$$
$$Y_{\text{shift}} = (0.937 \pm 0.006) Y_{\text{motor}} - (2.053 \pm 0.046)\ \mu\text{m}$$

where X_{shift} and Y_{shift} are the retrieved displacements, and X_{motor} and Y_{motor} are the imposed displacements. The slopes close to unity indicate that the imposed translations were recovered with good accuracy over the tested range.

We then evaluated the feasibility of the same registration technique in a more complete EP configuration. For this second test, a coverslip containing annular fluorescence targets (Invitrogen Focalcheck F7235, 15μm diameter) was bonded onto the SVEF. The assembled device was then integrated into the BIME and mounted on a

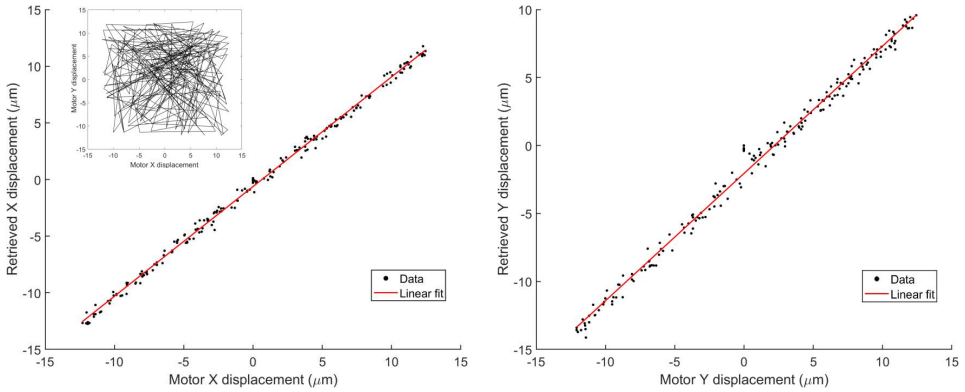


Fig. 5 Validation of SVEF-based motion retrieval. Retrieved displacements obtained by cross-correlation of the vascular pattern are plotted against the motor-imposed displacements along the x and y axes, respectively. The lattice of displacements (25×25 μm^2) is shown in the top-left corner. The solid red lines indicate the linear fits.

modified stage reproducing eye-like saccadic motion, following the method described in Fusco et al. [33]. This configuration allowed us to test the effect of SVEF-based registration on fluorescence-image reconstruction. The sample was illuminated with the LED channel for reflectance-based tracking and with a speckle laser illumination for fluorescence acquisition. The exposure time of both cameras was set to 2 ms to avoid motion blur during acquisition. A representative measurement is shown in Figure 6. Panel a) shows a single fluorescence frame, while panel b) shows the average of the registered frames. Registration of the image stack enabled multiple frames to be combined, improving the signal-to-noise ratio of the fluorescence image. After computing the average of the registered frames, we applied the reconstruction algorithm described in Capalbo et al. [37], namely the Gen-RL algorithm, for final image enhancement. The result is shown in panel c) and further illustrated by the intensity profiles in panels d) and e). Averaging the registered frames reduced noise-induced fluctuations in the intensity profiles, but did not resolve the anular structure of the fluorescence target. In contrast, after applying the Gen-RL algorithm, the two lobes and the central hole of the target became clearly distinguishable.

These results show that the SVEF provides a trackable vascular pattern suitable for validation of image-registration and motion-correction techniques. In addition, its integration within the BIME platform supports the use of the SVEF as a structural reference for multi-frame retinal imaging workflows, including fluorescence-image reconstruction and potential resolution-enhancement applications.

2.5 Compatibility with biological samples

To assess the compatibility of the SVEF platform with biological specimens, we performed an additional qualitative test using fixed human iPSC-derived retinal cultures. Retinal cells differentiated on 12-mm glass coverslips were stained for F-actin and

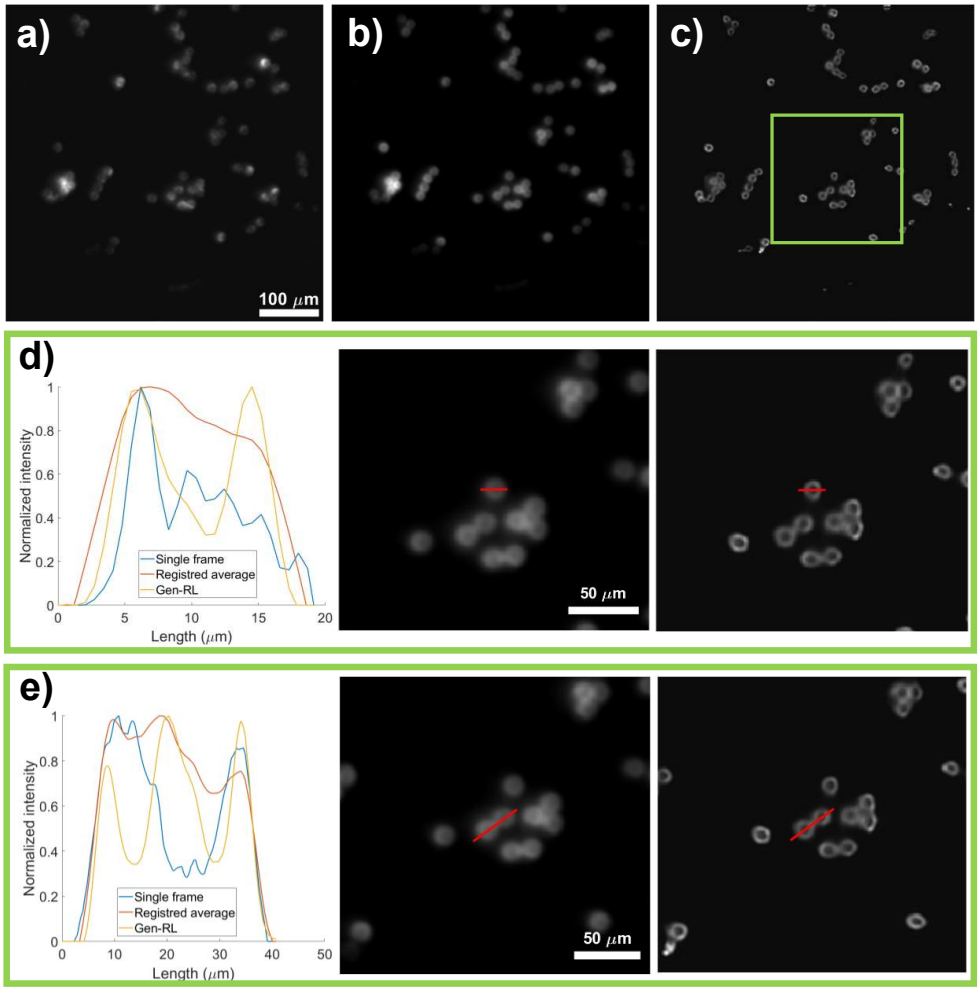


Fig. 6 Fluorescence-image reconstruction. **a)** Representative single fluorescence frame acquired from annular fluorescent targets (15 μm diameter) under random eye-like motion. **b)** Average of the registered fluorescence frames, obtained after estimating the frame displacements from the SVEF vascular pattern. **c)** Fluorescence image reconstructed using the Gen-RL algorithm [37]. The green box indicates the region enlarged in panels d) and e). **d), e)** Representative zoomed regions and corresponding normalized intensity profiles extracted along the red lines. The profiles compare the single frame, the registered average and the Gen-RL reconstruction. While the registered average reduces noise fluctuations, the Gen-RL reconstruction enables image enhancement, allowing the annular structure of the fluorescent targets to be clearly distinguished. Scale bars: 100 μm in panels a)-c) and 50 μm in panels d)-e).

nuclei, bonded onto the SVEF and mounted in the BIME sample holder. The assembled samples were then imaged by spinning-disk confocal microscopy, as described in the Methods section. The cultures remained attached to the coverslip during mounting and imaging, and fluorescent cellular structures were clearly detectable across the

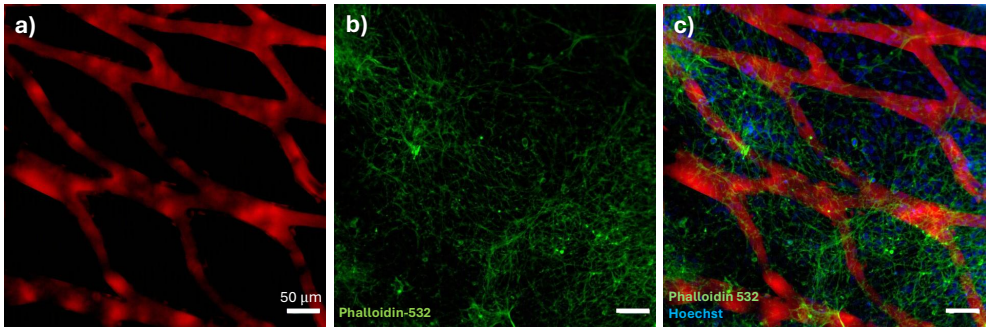


Fig. 7 Representative images of human iPSC-derived retinal neurons on the SVEF. **a)** Retinal-like vascular structures acquired using transmitted-light illumination and shown in red for visualization purposes. **b)** Fluorescence acquisition of human iPSC-derived retinal cultures labelled with the actin-binding protein Phalloidin 532 (green) to visualize the cellular network; nuclei counterstained with Hoechst (blue). **c)** Merged image of retinal neurons and retinal-like vascular structures, illustrating the compatibility of the SVEF platform with biological specimens. Scale bars are 50 µm.

acquired field of view. Representative images in Figure 7 showed Hoechst-positive nuclei and phalloidin-labelled structures, confirming that biological samples can be integrated with the SVEF assembly without preventing fluorescence acquisition. This experiment was intended as a qualitative compatibility test and supports the use of the SVEF as a structural fundus-like reference in model-eye experiments involving fluorescent biological specimens.

3 Discussion

We developed and characterized a Synthetic Vascularized Eye Fundus designed as a perfusable and contrast-tunable fundus insert for EP platforms. The device combines a photolithographically defined microfluidic vascular network with a scattering substrate and hemoglobin-based perfusion, thereby producing absorbing vessel-like structures against a bright diffuse background. The comparison between standard PDMS and PDMS–ZnO confirmed the importance of the scattering substrate for vessel visualization under reflectance illumination, showing that the improved vascular contrast arises from the optical background provided by the composite material. Optimization of hemoglobin perfusion showed that the vascular contrast of the SVEF could be tuned by changing the absorber concentration. Among the tested conditions, the 2 mM hemoglobin solution produced a mean contrast closest to that measured in a representative human fundus image, while higher concentrations generated stronger vessel contrast. This result supports hemoglobin perfusion as a simple and adjustable strategy to adapt the optical appearance of the device to different imaging requirements. The measured apparent microchannel widths were compatible with the size range of small retinal vessels, indicating that microscale vessel-like features remain detectable after fabrication, perfusion and integration into the BIME platform.

The SVEF also provided a stable structural pattern for image-registration experiments based on cross-correlation of the vascular network. In a complete EP configuration including saccade-like motion, the device supported multi-frame fluorescence acquisition and subsequent image reconstruction. This demonstrates that the vascular pattern can serve as an auxiliary structural reference when the fluorescence signal itself is weak, sparse or not optimal for direct registration. This aspect is particularly relevant in retinal imaging, where involuntary eye movements can degrade multi-frame acquisitions and where registration is often required before averaging, comparing across time or computational reconstructing.

The qualitative experiment with fixed human iPSC-derived retinal cultures further showed that biological specimens can be integrated with the SVEF assembly without preventing fluorescence imaging. Although this experiment was not intended as a quantitative biological validation, it supports the compatibility of the platform with fluorescent biological samples and suggests that the SVEF may be used as a structural fundus-like reference in model-eye experiments involving labelled retinal specimens.

Several limitations should be considered. The current device reproduces a simplified vascular and optical environment and does not include the multilayered anatomy, wavelength-dependent scattering or dynamic perfusion properties of the human fundus. In addition, hemoglobin solutions approximate vascular absorption but do not fully reproduce the optical behaviour of whole blood. However, the SVEF was not intended to reproduce the full biological, spectral or optical complexity of the human fundus. It is intentionally distinct from retinal phantoms designed to maximize anatomical fidelity. Recent systems have reproduced multilayer retinal anatomy and multiple vascular plexuses and have been demonstrated across several ophthalmic imaging modalities. The purpose of the SVEF is instead to provide a simple, controllable vascular reference whose optical contrast and imposed motion can be experimentally defined. Its integration into BIME additionally allows the same vascular pattern to be used for reflectance-based motion tracking while fluorescence signals are acquired from a separate target or biological specimen. This combination makes the platform particularly suited to benchmarking registration, multi-frame reconstruction and cross-modal imaging workflows under controlled model-eye conditions.

4 Methods

4.1 Photomask design and master mold fabrication

The microfluidic layout was designed in KLayout [38] and exported in GDSII format for mask fabrication. The device footprint was defined as a 12 mm-diameter circle with a 2 mm-diameter inlet included for fluidic interfacing and outlets implemented as terminal vessel ends. A structured micro-grid was superimposed onto the central vascular structure to provide a dense array of intersection points intended as preferential sites for cell positioning and signal acquisition within the imaging field of view. Photomask was fabricated by an external service (Christian Koenen GmbH, Ottobrunn, Germany) on high-stability polyester film with a printing resolution of 25,000 PPI to minimize edge aliasing and preserve the critical dimensions of the microchannels and grid features. SU-8 3025 (Kayaku Advanced Materials, Westborough, MA, USA), a negative

photoresist, was used to fabricate the master mold on glass substrates (50 × 50 mm, thickness 1 mm). The master molds were fabricated using standard photo-lithography protocol.

UV exposure was performed using a UV-KUB 2 mask aligner/exposure system (KLOÉ S.A.S., Montpellier, France) in "Masking" mode. Exposure was delivered at 65% power intensity for 25 s.

Post-exposure bake was used to drive the acid-catalyzed crosslinking reaction in exposed regions: 65°C for 1 min, 95°C for 7 min, then 65°C for 1 min, to reduce stress and pattern distortion. To pattern the high-density vascular network, development was performed in SU-8 developer (PGMEA-based) using a low-shear protocol to prevent delamination and mechanical damage of dense microstructures. For grid-containing regions, the IPA rinse was carefully directed over the vascular network using a plastic Pasteur pipette to facilitate removal of undeveloped resist trapped within grid interstices while minimizing lateral shear. The sample was visually inspected after rinsing; the absence of white streaks/residue during the IPA rinse confirmed the process completion. The master mold was then dried under nitrogen. To increase mechanical durability for repeated replica molding cycles, the developed SU-8 master mold was hard-baked at 65°C for 1 min, 95°C for 1 min, then at 150°C for 90 min.

4.2 PDMS replica molding and chip sealing

Microfluidic chips were fabricated from the SU-8 master mold by replica molding using polydimethylsiloxane (PDMS; Sylgard 184 Silicone Elastomer Kit, Dow, Midland, MI, USA). Standard PDMS is highly transparent in the visible range and exhibits negligible intrinsic scattering, which limits back-scattered signal under reflectance imaging [28]. Therefore, to reproduce a fundus-like scattering background, PDMS was modified by adding Zinc Oxide (ZnO) nanopowder (Sigma-Aldrich; particle size ¡ 100 nm), yielding an opaque, diffusely reflecting composite substrate. This modification was intended to mimic posterior-eye scattering properties, rather than the biochemical origin of fundus autofluorescence [4].

ZnO was selected because its refractive index, n, is substantially higher than that of PDMS [32] ($n_{PDMS} \sim 1.41$, $n_{ZnO} \sim 2$), producing strong light scattering from refractive-index mismatch within the polymer. The filler was added at a 1:10 weight ratio (ZnO:PDMS prepolymer), yielding an opaque white elastomer. The PDMS base and curing agent were mixed at a 10:1 weight ratio and centrifuged at 1400 rpm for 15 min to promote homogenization. ZnO nanopowder was then added into the PDMS prepolymer followed by vigorous mixing on a vortex shaker for $\sim$ 30 s to disrupt agglomerates and facilitate a uniform suspension. The composite was subsequently degassed in a vacuum chamber for $\sim$ 20 min to remove entrapped air introduced during mixing. The degassed PDMS–ZnO composite was poured onto the SU-8 master mold to a thickness of 1–2 mm and degassed again to ensure bubble-free replication at the master interface. Samples were cured in an oven at 70°C for 2 h, cooled to room temperature, and carefully demolded. To minimize stress on the SU-8 microstructures, the slab perimeter was first trimmed with a scalpel, detachment was initiated with a thin metal spatula, and the replica was peeled off slowly at a low angle ($< 45°$). Using a biopsy punch, the cured replica was shaped into a 12 mm-diameter disk and an inlet

reservoir was created. Microchannels were sealed by plasma bonding to a clean 12 mm-diameter glass coverslip. Surfaces were activated by oxygen plasma treatment (high power, 3 min), brought into conformal contact immediately after plasma exposure to form covalent siloxane bonds, and baked on a hotplate at 50°C for 20 min to enhance bond strength.

4.3 Perfusion medium and microchannel filling

To generate a fundus-like vascular contrast under reflectance illumination while maintaining compatibility with fluorescence imaging, the microfluidic network was perfused with an aqueous hemoglobin solution prepared from lyophilized bovine hemoglobin (Sigma-Aldrich, St. Louis, MO, USA). The solution was prepared in distilled water at different concentrations (i.e., 2, 2.5 and 3 mM) and gently mixed until fully homogeneous. Microchannels were filled using a syringe-pump perfusion setup. A programmable syringe pump (Pump 11 Elite, Harvard Apparatus, Holliston, MA, USA) equipped with a 1 mL disposable syringe was connected to the device inlet via polytetrafluoroethylene (PTFE) tubing (outer diameter 1.6 mm, inner diameter 0.8 mm; Dolomite Microfluidics, Royston, UK) using a Luer-lock adapter to ensure leak-free operation. The pump was operated in infuse-only mode at a constant flow rate of 10 μL/min. Perfusion was continued until complete filling of the vascular network was visually confirmed, including the central grid region. To enable integration of the SVEF within the BIME platform, the perfused device was rendered leak-tight prior to immersion in the water-filled chamber (vitreous-humor mimic).

The microfluidic design includes multiple outlet terminations at the chip boundary to facilitate low-resistance filling and air evacuation; however, these open outlets would allow exchange between the perfused contrast medium and the surrounding aqueous environment during operation. Therefore, a post-perfusion sealing step was implemented to confine the contrast agent within the vascular network and prevent dilution or leakage upon submersion. After completing perfusion with the hemoglobin solution, the syringe pump was stopped to equilibrate pressure. Norland Optical Adhesive 61 (NOA 61; Norland Products Inc., Cranbury, NJ, USA) was then applied as a narrow bead along the edge of the chip to cover the outlet terminations, and a small amount was also applied to seal the inlet port. Due to its high viscosity, the adhesive does not penetrate into the microchannels. The applied NOA 61 was cured using long-wave UV illumination (365 nm) for ~ 60 s, producing a transparent, mechanically stable seal.

4.4 Microchannel width analysis

Microchannel width was estimated from transverse intensity profiles extracted across perfused channels. Since the hemoglobin-filled channels appeared darker than the surrounding PDMS–ZnO background, each profile was normalized to the local background and inverted so that the channel corresponded to a positive signal. The local background intensity was estimated from the lateral portions of the profile, corresponding to the first and last 10% of sampled points. The normalized and inverted profile was fitted with a parametric double-edge model representing the channel as a plateau

Table 2 Vessel width computed for the SVEF devices perfused with 2mM hemoglobin concentration and imaged with a fundus imaging module [3]. The ID corresponds to the profiles shown in the right panel in Figure 3.

Profile ID	Width (μm)	RMSE error
1	19.61	0.06
2	43.60	0.06
3	34.19	0.05
4	14.81	0.06
5	48.46	0.04
6	24.31	0.04
7	18.20	0.06

bounded by two smooth transitions:

$$y(x) = B(x) + A\left[S(x; x_L, \sigma) - S(x; x_R, \sigma)\right], \tag{2}$$

where x is the position along the transverse profile, $B(x) = b_0 + b_1 x$ is a slowly varying linear background, A is the channel signal amplitude, x_L and x_R are the fitted positions of the left and right channel edges, and σ describes the smoothness of the edge transitions. The transition function S was modelled as an error-function edge:

$$S(x; x_0, \sigma) = \frac{1}{2}\left[1 + \operatorname{erf}\left(\frac{x - x_0}{\sqrt{2}\sigma}\right)\right]. \tag{3}$$

For each profile, the channel width was defined as the distance between the two fitted edge positions:

$$W = x_R - x_L. \tag{4}$$

The goodness of fit was assessed using the root mean square error (RMSE) between the normalized measured profile and the fitted profile:

$$\mathrm{RMSE} = \sqrt{\frac{1}{N}\sum_{i=1}^{N}(y_i - \hat{y}_i)^2}, \tag{5}$$

where y_i is the measured normalized profile, $\hat{y}_i$ is the fitted profile, and N is the number of sampled points. The width and RMSE values across the selected profiles (see Figure 3) are reported in Table 2.

4.5 Human iPSCs differentiation into retinal neuron

Retinal cultures were generated from a healthy human iPSC line following Sluch et al. [39], with minor modifications. iPSCs were dissociated to single cells with Accutase (Gibco) and seeded into Matrigel coated dishes (Corning, 1:100) at 100.000 cells/cm^2 in mTeSR™ Plus with 10 μM Y 27632 (PeproTech). After 24 h, medium was changed

to N2B27 w/o vitamin A (50% DMEM/F 12, 50% Neurobasal, GlutaMAX, pen strep, NEAA, N2, B27 w/o A) and cultured up to DIV30. To induce retinal differentiation, a different mix of small molecules was added as follows: dorsomorphin 1 μM and IDE2 2.5 μM (DIV 0–6); nicotinamide 10 mM (until DIV 10); forskolin 25 μM (DIV 0–30); DAPT 10 μM (DIV 20–30). The retinal cells were plated onto PLO/Laminin (Sigma-Aldrich) coated round cover glasses (Ø 12mm, Thorlabs, Newton, New Jersey, Stati Uniti) at a density of 150000 cells per glass for subsequent experiments.

4.6 Immunostaining and confocal spinning-disk imaging of iPSC-derived retinal neurons

iPSC-derived retinal neurons were fixed at day in vitro (DIV) 30 with 4% paraformaldehyde (PFA; Sigma-Aldrich) for 15 min at room temperature. Fixed cells were permeabilized with PBS containing 0.2% Triton X 100 (Sigma-Aldrich) for 10 min and incubated for 45 min in blocking solution (PBS, 0.1% Tween 20, Sigma-Aldrich, and 5% goat serum, Merck KGaA). Samples were incubated with Phalloidin Atto 532 (1:30, 49429, Sigma-Aldrich) for 1 h at room temperature; nuclei were stained with Hoechst 33342 (1:300, 33258, Merck). Prepared samples were mounted on the SVEF using DAKO Fluorescent Mounting Medium (Sigma-Aldrich). Fluorescence images were acquired with a spinning disk confocal (X Light V3, CrestOptics) using a 20× air objective (NA 0.42, Olympus), a PRIME sCMOS camera (Crisel Instruments), and MetaMorph software (Molecular Devices).

4.7 Human fundus measurements

Fundus measurements from human participants were acquired using the fundus imaging module described by Salajková et al. [3], under a clinical trial registered on ClinicalTrials.gov on 24 February 2025 (ID: NCT06841848, https://clinicaltrials.gov/study/NCT06841848?term=NCT06841848&rank=1).

Funding. This research was funded by the Italian Fund for Applied Sciences (FISA) of the Italian Ministry of University and Research (MUR), under Call No. 1233 of August 1, 2023 (project "ROAD- Retina Observation for Alzheimer Diagnostic", CUP B83D23001150001).

Author contributions. M.L. conceived the study. V.C., G.G., Z.S., O.B., M.G.G., M.G., M.F., A.Z., M.G., R.R., Y.G. and S.D.A. contributed to the experimental work and data acquisition. V.C. and G.G. performed the data analysis and wrote the main manuscript text. G.R. contributed to funding acquisition and supervised the study. All authors contributed to the discussion of the results and reviewed and approved the final manuscript.

Competing interests. The authors declare no competing interests.

Data availability. Data presented in this paper are not publicly available but may be obtained from the corresponding author upon reasonable request.

References

[1] Burns, S.A., Elsner, A.E., Gast, T.J.: Imaging the retinal vasculature. Annual Review of Vision Science **7**, 129–153 (2021) https://doi.org/10.1146/annurev-vision-093019-113719

[2] Snyder, P.J., Alber, J., Alt, C., Bain, L.J., Bouma, B.E., Bouwman, F.H., DeBuc, D.C., Campbell, M.C.W., Carrillo, M.C., Chew, E.Y., Cordeiro, M.F., Dueñas, M.R., Fernández, B.M., Koronyo-Hamaoui, M., La Morgia, C., Carare, R.O., Sadda, S.R., Wijngaarden, P., Snyder, H.M.: Retinal imaging in alzheimer's and neurodegenerative diseases. Alzheimer's & Dementia **17**(1), 103–111 (2021) https://doi.org/10.1002/alz.12179

[3] Salajková, Z., Ciasca, G., Di Lorenzo, F., Ghoreishi, M., Reale, R., Gambarota, M.G., Zhang, J., Zhang, Y., Ricco, V., Ruocco, G., Leonetti, M.: Non-invasive screening of alzheimer's disease via label-free tri-spectral retinal imaging. Scientific Reports **16**(1), 5083 (2026) https://doi.org/10.1038/s41598-026-35383-y

[4] Schmitz-Valckenberg, S., Pfau, M., Fleckenstein, M., Staurenghi, G., Sparrow, J.R., Bindewald-Wittich, A., Spaide, R.F., Wolf, S., Sadda, S.R., Holz, F.G.: Fundus autofluorescence imaging. Progress in Retinal and Eye Research **81**, 100893 (2021) https://doi.org/10.1016/j.preteyeres.2020.100893

[5] Sauer, L., Vitale, A.S., Modersitzki, N.K., Bernstein, P.S.: Fluorescence lifetime imaging ophthalmoscopy: autofluorescence imaging and beyond. Eye **35**(1), 93–109 (2021) https://doi.org/10.1038/s41433-020-01287-y

[6] Koronyo, Y., Biggs, D., Barron, E., Boyer, D.S., Pearlman, J.A., Au, W.J., Kile, S.J., Blanco, A., Fuchs, D.-T., Ashfaq, A., Frautschy, S., Cole, G.M., Miller, C.A., Hinton, D.R., Verdooner, S.R., Black, K.L., Koronyo-Hamaoui, M.: Retinal amyloid pathology and proof-of-concept imaging trial in Alzheimer's disease. JCI Insight **2**(16), 93621 (2017) https://doi.org/10.1172/jci.insight.93621

[7] Cao, K.J., Kim, J.H., Kroeger, H., Gaffney, P.M., Lin, J.H., Sigurdson, C.J., Yang, J.: Arcam-1 facilitates fluorescence detection of amyloid-containing deposits in the retina. Translational Vision Science & Technology **10**(7), 5 (2021) https://doi.org/10.1167/tvst.10.7.5

[8] Soloperto, A., Quaglio, D., Baiocco, P., Romeo, I., Mori, M., Ardini, M., Presutti, C., Sannino, I., Ghirga, S., Iazzetti, A., Ippoliti, R., Ruocco, G., Botta, B., Ghirga, F., Di Angelantonio, S., Boffi, A.: Rational design and synthesis of a novel bodipy-based probe for selective imaging of tau tangles in human ipsc-derived cortical neurons. Scientific Reports **12**(1), 5257 (2022) https://doi.org/10.1038/s41598-022-09016-z

[9] Javed, A., Khanna, A., Palmer, E., Wilde, C., Zaman, A., Orr, G., Kumudhan, D., Lakshmanan, A., Panos, G.D.: Optical coherence tomography angiography: a

review of the current literature. Journal of International Medical Research **51**(7), 3000605231187933 (2023) https://doi.org/10.1177/03000605231187933

[10] Atchison, D.A., Smith, G.: Optics of the Human Eye. Butterworth-Heinemann, Oxford (2000). https://doi.org/10.1016/B978-0-7506-3775-6.X5001-9

[11] Liang, J., Williams, D.R., Miller, D.T.: Supernormal vision and high-resolution retinal imaging through adaptive optics. Journal of the Optical Society of America A **14**(11), 2884–2892 (1997) https://doi.org/10.1364/JOSAA.14.002884

[12] Sánchez Brea, L., Andrade De Jesus, D., Shirazi, M.F., Pircher, M., Walsum, T., Klein, S.: Review on retrospective procedures to correct retinal motion artefacts in oct imaging. Applied Sciences **9**(13), 2700 (2019) https://doi.org/10.3390/app9132700

[13] Ramli, R., Hasikin, K., Idris, M.Y.I., A. Karim, N.K., Wahab, A.W.A.: Fundus image registration technique based on local feature of retinal vessels. Applied Sciences **11**(23), 11201 (2021) https://doi.org/10.3390/app112311201

[14] Nie, Q., Zhang, X., Hu, Y., Gong, M., Liu, J.: Medical image registration and its application in retinal images: a review. Visual Computing for Industry, Biomedicine, and Art **7**, 21 (2024) https://doi.org/10.1186/s42492-024-00173-8

[15] Peli, E., Augliere, R.A., Timberlake, G.T.: Feature-based registration of retinal images. IEEE Transactions on Medical Imaging **6**(3), 272–278 (1987) https://doi.org/10.1109/TMI.1987.4307837

[16] Bruin, D.M., Bremmer, R.H., Kodach, V.M., Kinkelder, R., Marle, J., Leeuwen, T.G., Faber, D.J.: Optical phantoms of varying geometry based on thin building blocks with controlled optical properties. Journal of Biomedical Optics **15**(2), 025001 (2010) https://doi.org/10.1117/1.3369003

[17] Luu, L., Roman, P.A., Mathews, S.A., Ramella-Roman, J.C.: Microfluidics based phantoms of superficial vascular network. Biomedical Optics Express **3**(6), 1350–1364 (2012) https://doi.org/10.1364/BOE.3.001350

[18] Ghassemi, P., Wang, J., Melchiorri, A.J., Ramella-Roman, J.C., Mathews, S.A., Coburn, J.C., Sorg, B.S., Chen, Y., Pfefer, T.J.: Rapid prototyping of biomimetic vascular phantoms for hyperspectral reflectance imaging. Journal of Biomedical Optics **20**(12), 121312 (2015) https://doi.org/10.1117/1.JBO.20.12.121312

[19] Mishra, S., Thakur, A., Redenti, S., Vázquez, M.: A model microfluidics-based system for the human and mouse retina. Biomedical Microdevices **17**(6), 107 (2015) https://doi.org/10.1007/s10544-015-0002-6

[20] Lee, H.-J., Samiudin, N.M., Lee, T.G., Doh, I., Lee, S.-W.: Retina phantom for the evaluation of optical coherence tomography angiography based on microfluidic

channels. Biomed. Opt. Express **10**(11), 5535–5548 (2019) https://doi.org/10.1364/BOE.10.005535

[21] Zhao, X., Zhang, Y., Liu, H., Wang, J., Chen, Y., Li, Z.: Rapid prototyping of a retinal multivascular network phantom for optical retinal vascular imaging equipment evaluation. Biomedical Optics Express **15**(7), 4253–4263 (2024) https://doi.org/10.1364/BOE.523115

[22] Lee, H.-J., Lee, T.G., Doh, I., Lee, S.-W.: Design and application of a realistic and multifunctional retinal phantom for standardizing ophthalmic imaging systems. Communications Engineering **4**(1), 134 (2025) https://doi.org/10.1038/s44172-025-00475-6

[23] Ferraro, G., Gigante, Y., Pitea, M., Mautone, L., Ruocco, G., Di Angelantonio, S., Leonetti, M.: A model eye for fluorescent characterization of retinal cultures and tissues. Scientific Reports **13**(1), 10983 (2023) https://doi.org/10.1038/s41598-023-37806-6

[24] Mack, C.: Fundamental principles of optical lithography: The science of microfabrication. John Wiley & Sons, Ltd (2007). https://doi.org/10.1002/9780470723876

[25] Fayed, A.E., Menten, M.J., Kreitner, L., Paetzold, J.C., Rueckert, D., Bassily, S.M., Fikry, R.R., Hagag, A.M., Sivaprasad, S.: Retinal vasculature of different diameters and plexuses exhibit distinct vulnerability in varying severity of diabetic retinopathy. Eye (Lond) **38**(9), 1762–1769 (2024) https://doi.org/10.1038/s41433-024-03021-4

[26] Duffy, D.C., McDonald, J.C., Schueller, O.J.A., Whitesides, G.M.: Rapid prototyping of microfluidic systems in poly(dimethylsiloxane). Analytical Chemistry **70**(23), 4974–4984 (1998) https://doi.org/10.1021/ac980656z

[27] McDonald, J.C., Duffy, D.C., Anderson, J.R., Chiu, D.T., Wu, H., Schueller, O.J.A., Whitesides, G.M.: Fabrication of microfluidic systems in poly(dimethylsiloxane). Electrophoresis **21**(1), 27–40 (2000) https://doi.org/10.1002/(SICI)1522-2683(20000101)21:1⟨27::AID-ELPS27⟩3.0.CO;2-C

[28] Ariati, R., Sales, F., Souza, A., Lima, R.A., Ribeiro, J.: Polydimethylsiloxane composites characterization and its applications: A review. Polymers **13**(23), 4258 (2021) https://doi.org/10.3390/polym13234258

[29] Wróbel, M.S., Popov, A.P., Bykov, A.V., Kinnunen, M., Jędrzejewska-Szczerska, M., Tuchin, V.V.: Multi-layered tissue head phantoms for noninvasive optical diagnostics. Journal of Innovative Optical Health Sciences **8**(3), 1541005 (2015) https://doi.org/10.1142/S1793545815410059

[30] Campo, A., Greiner, C.: Su-8: a photoresist for high-aspect-ratio and 3d submicron lithography. Journal of Micromechanics and Microengineering **17**(6), 81–95

(2007) https://doi.org/10.1088/0960-1317/17/6/R01

[31] Piruska, A., Nikcevic, I., Lee, S.H., Ahn, C., Heineman, W.R., Limbach, P.A., Seliskar, C.J.: The autofluorescence of plastic materials and chips measured under laser irradiation. Lab on a Chip **5**(12), 1348–1354 (2005) https://doi.org/10.1039/b508288a

[32] Al-Kuhaili, M.F., Durrani, S.M.A., El-Said, A.S., Heller, R.: Enhancement of the refractive index of sputtered zinc oxide thin films through doping with fe2o3. Journal of Alloys and Compounds **690**, 453–460 (2017) https://doi.org/10.1016/j.jallcom.2016.08.165

[33] Fusco, D., Xypakis, E., Gigante, Y., Mautone, L., Di Angelantonio, S., Ponsi, G., Ruocco, G., Leonetti, M.: Stochastically structured illumination microscopy scan less super resolution imaging. npj Imaging **2**(1), 45 (2024) https://doi.org/10.1038/s44303-024-00047-x

[34] Faber, D.J., Aalders, M.C.G., Mik, E.G., Hooper, B.A., Gemert, M.J.C., Leeuwen, T.G.: Oxygen saturation-dependent absorption and scattering of blood. Physical Review Letters **93**(2), 028102 (2004) https://doi.org/10.1103/PhysRevLett.93.028102

[35] Bosschaart, N., Edelman, G.J., Aalders, M.C.G., Leeuwen, T.G., Faber, D.J.: A literature review and novel theoretical approach on the optical properties of whole blood. Lasers in Medical Science **29**(2), 453–479 (2014) https://doi.org/10.1007/s10103-013-1446-7

[36] Billett, H.H.: Hemoglobin and hematocrit. In: Walker, H.K., Hall, W.D., Hurst, J.W. (eds.) Clinical Methods: The History, Physical, and Laboratory Examinations, 3rd edn. Butterworths, Boston (1990). https://www.ncbi.nlm.nih.gov/books/NBK259/

[37] Capalbo, V., Battaglini, D., Petroni, M., Ruocco, G., Leonetti, M.: Translation-based structured illumination microscopy via the generalized richardson-lucy method. Optics Express **33**(14), 30607–30620 (2025) https://doi.org/10.1364/OE.563690

[38] Köfferlein, M.: KLayout Layout Viewer and Editor. https://www.klayout.de (2026)

[39] Sluch, V.M., Chamling, X., Liu, M.M., Berlinicke, C.A., Cheng, J., Mitchell, K.L., Welsbie, D.S., Zack, D.J.: Enhanced stem cell differentiation and immunopurification of genome engineered human retinal ganglion cells. Stem Cells Translational Medicine **6**(11), 1972–1986 (2017) https://doi.org/10.1002/sctm.17-0059